

**Citation for published version:**

Kaddour Fouad, Houari Merabet Boulouiha, Ahmed Allali, Ali Taibi, and Mouloud Denai, 'Multivariable control of a grid-connected wind energy conversion system with power quality enhancement', *Energy Systems*, Vol. 9 (1): 25-57, February 2018.

**DOI:**

<https://doi.org/10.1007/s12667-016-0223-7>

**Document Version:**

This is the Accepted Manuscript version.

The version in the University of Hertfordshire Research Archive may differ from the final published version.

**Copyright and Reuse:**

© 2016 Springer-Verlag Berlin Heidelberg.

Content in the UH Research Archive is made available for personal research, educational, and non-commercial purposes only. Unless otherwise stated, all content is protected by copyright, and in the absence of an open license, permissions for further re-use should be sought from the publisher, the author, or other copyright holder.

**Enquiries**

If you believe this document infringes copyright, please contact Research & Scholarly Communications at [rsc@herts.ac.uk](mailto:rsc@herts.ac.uk)

# Multivariable Control of a Grid-Connected Wind Energy Conversion System with Power Quality Enhancement

<sup>1</sup>Kaddour Fouad, <sup>2</sup>Houari Merabet Boulouiha, <sup>1</sup>Ahmed Allali, <sup>3</sup>Ali Taibi, <sup>4</sup>Mouloud Denai

<sup>1</sup>LDDEE, Laboratoire de Developpement Durable de l'Energie Electrique

University of Science and Technology of Oran, Department of Electrotechnics, Algeria

<sup>2</sup>University Centre of Relizane, Algeria

<sup>3</sup>IUT de Tremblay en France Paris 8

<sup>4</sup>School of Engineering & Technology, University of Hertfordshire, Hatfield AL10 9AB, UK

**Abstract** – This paper proposes the design of a multivariable robust control strategy for a variable-speed WECS based on a SCIG.

Optimal speed control of the SCIG is achieved by a conventional PI controller combined with a MPPT strategy. DTC-SVM technique based on a simple Clarke transformation is used to control the generator-side three-level converter in the variable speed WECS. The flow of real and reactive power between the inverter and the grid is controlled via the grid real and reactive currents and the DC link voltage using multivariable  $H_\infty$  control. The overall WECS and control scheme are developed in Matlab/Simulink and the performance of the proposed control strategy is evaluated via a set of simulation scenarios replicating various operating conditions of the WECS such as variable wind speed and asymmetric single grid faults. The power quality of the WECS system under  $H_\infty$  control approach is assessed and the results show a significant improvement in the total harmonic distortion as compared to that achieved with a classical PI control.

**Keywords:** Wind energy, squirrel cage induction generator, direct torque control, space vector PWM, MPPT,  $H_\infty$  control, multilevel inverter .

## List of symbols and abbreviations

PI	Proportional Integral
MPPT	Maximum Power Point Tracking
LMI	Linear Matrix Inequality
AC	Alternative Current
DC	Direct Current
PMSG	Permanent Magnet Synchronous Generator
SVM	Space Vector Modulation
SCIG	Squirrel Cage Induction Generator
DFIG	Doubly Fed Induction Generator
MI	Modulation Index
WECS	Wind Energy Conversion System
DTC	Direct Torque Control
DTFC	Direct Torque and Flux Control
PLL	Phase Locked Loop
PWM	Pulse Width Modulation
NPC	Neutral Point Clamped
DTC-SVPWM	Direct Torque Control Space Vector Pulse Width Modulation

## 1. Introduction

Wind energy has the potential to play a significant role in achieving the world's future energy targets. It is currently amongst the fastest-growing renewable energy technologies. The total installed capacity around the world was estimated to 296,255 MW in 2013 which represents 3.5% of the global electricity demand [1].

Extensive ongoing research has been done on WECS configurations combining various wind turbine technologies and generator types. [2]. There are many different types of generators used today in WECS [3] The most common types are the SCIG [4] and the DFIG [5-6]. In recent years, PMSG are gaining popularity in WECS applications due to their higher reliability and efficiency [7-9].

There are essentially two operating regions for wind turbines: In the partial load region, wind speed is not fast enough to produce the rated power. In this region, the main control objective is to track the maximum power coefficient ( $C_{Pmax}$ ) to extract the full power from the wind. The pitch angle is usually fixed in this region and the generator torque is adjusted to control the rotational speed and keep the operating point close to  $C_{Pmax}$ . In the full load region, wind speed is above the rated value and wind power exceeds the rated power of the generator. The captured power is controlled by using aerodynamic power control of the rotor by adjusting the pitch angle of the blades and hence reducing the power coefficient  $C_p$  of the rotor.

Several methods have been proposed for the control of WECSs ranging from classical control methods [10] which are currently the most widely used methods in real applications to more advanced control strategies which have been the subject of active research in the past few years [11].

WECS are complex mechanical structures which exhibit nonlinear dynamics and are continuously subjected to disturbances such as uncontrolled wind profiles, wind shear and tower shadows effects. In addition, mathematical models describing accurately the turbine dynamics are difficult to obtain which makes control design a challenging task. The aim of this contribution is to design robust control strategies to overcome the problems associated with system parameter uncertainties and various disturbances such as those which may occur in a typical wind energy conversion system connected to the grid.

Robust control theory has been an active area of research in the last three decades. Robust control attempts to addresses both performance and stability criteria of a control system. Briefly, robustness is described as the ability of a controller to exhibit the desired performances for both the nominal model of the system and for any model contained within the set of models bounded by the specified range of models' uncertainties.

The application of robust control strategies to pitch angle control of a wind turbine was studied in [6]. In [12] the author proposed the design of a robust controller based on  $H_\infty$  for a simplified model of a turbine and generator system. The design of a robust controller based on gain-scheduling for a tidal turbine was proposed in [13]. The authors in [14] presented a comparative study between a PI classical controller and an  $H_\infty$  controller for the control of the frequency in a hybrid multi-source system including a wind turbine generator, diesel generators and fuel cells with electrolyzer. The synthesis of the  $H_\infty$  controller was based on the two standard approaches namely the LMI and loop shaping. In [15], a new hybrid robust control methodology is developed based on a fuzzy logic observer. The control scheme is applied to wind turbine system taking into account parameters uncertainties and external disturbance.

This paper proposes a hybrid design approach to solve the standard  $H_\infty$  problem based on LMI and loop shaping. The controller is applied to the control of the grid side currents and DC link voltage.

MPPT algorithms are used to maximise power extraction from wind energy by operating wind turbines at their optimal speed [16]. Different MPPT methods have been proposed for variable-speed WECS [17]. The method

used in this work is based on the knowledge of the aerodynamic characteristics of the wind turbine. A 2D look-up table is used to store the wind speed values and corresponding maximum power points.

The SCIG is driven by a variable-speed wind turbine which operates at maximum power under the MPPT strategy. The optimal speed output from the MPPT will represent the reference for the DTC-SVPWM of the converter [18]. Furthermore, a three-level NPC inverter topology is proposed, to enhance the energy efficiency and quality of the overall system WECS.

The AC side converter is controlled by a SVPWM and regulates both the DC voltage level and the active ( $i_d$ ) and reactive ( $i_q$ ) currents and subsequently the power flow in the utility grid. The reference used for the DC side voltage is larger than the forward voltage of the source and the reference value for the reactive current is set to zero to achieve a unity power factor.

The proposed robust multivariable controller based on  $H_\infty$  is designed and evaluated on a comprehensive model of the WECS and implemented using Matlab/Simulink and SimPowerSystems. A series of simulation results are presented to show the performance and robustness of the proposed control scheme under different operating conditions of the system.

The paper is organized as follows: Section 2 provides a detailed description of the WECS models and a derivation of the control strategies for the MPPT and the SCIG. Section 3 presents the design steps of the DTC-SVPWM for the three level inverter. Section 4 presents the aerodynamic protection against high wind speeds which was provided by pitch control. Section 5 presents the design of the  $H_\infty$  multivariable control concept for the grid-side currents and DC link voltage. Simulation results and conclusions are presented in Sections 6 and 7 respectively. The mathematical model of the DC link, grid-side currents are presented in the appendices together with the values of the model parameters used in the simulation.

## 2. CONFIGURATION OF THE VARIABLE-SPEED WIND ENERGY POWER SYSTEM

The structure of the WECS considered in this study is presented in Fig. 1. The three-bladed wind turbine and the SCIG are connected to the grid via a two three-level NPC-based AC/DC/AC converters [18].

The generator-side converter (converter 1) works as a rectifier and supplies the DC bus.

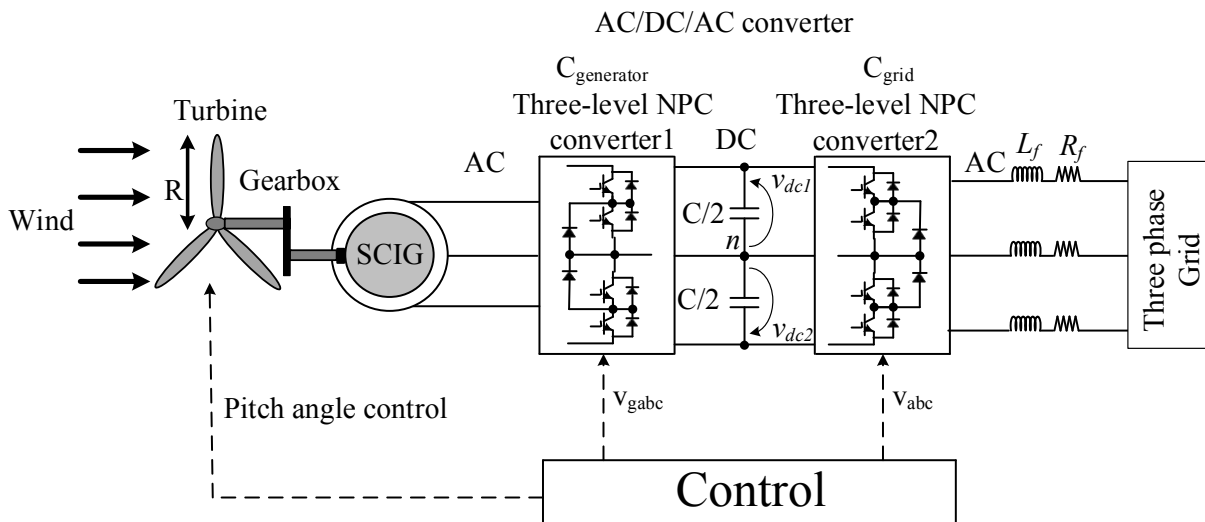


Fig. 1 Configuration of the SCIG-based WECS.

The grid-converter, labelled Converter 2 in Fig. 1, controls both the amplitude of the DC bus voltage, and the active and reactive power flow by adjusting two parameters of the SVPWM, namely, the MI and the phase shift



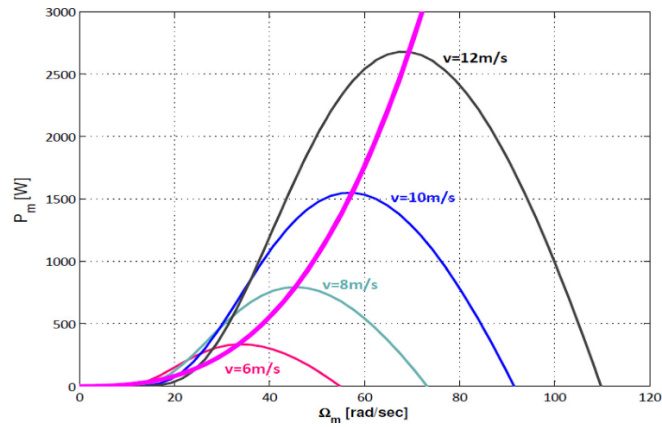


Fig. 3 Maximum power characteristics of the wind turbine.

#### 4. CONTROL OF AERODYNAMIC PROTECTION

The timing angle control is aimed to limit the power taken by adjusting the pitch angle  $\beta$  of the blades. The positioning mechanism is to guide blades towards a reference angle ( $\beta_{ref}$ ) via a hydraulic or electric system. The choice of this angle is usually achieved via an external loop to regulate either the speed of the turbine or the mechanical power generated. In our model, the latter method is used to generate the reference of the pitch angle ( $\beta_{ref}$ ). The system is thus be represented as follows:

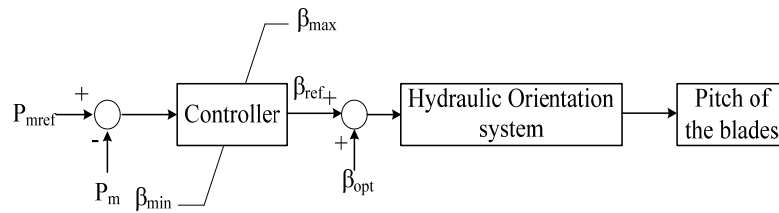


Fig. 4 Control of the mechanical power  $P_m$ .

Fig. 5 shows a 3D graphical representation of the power coefficient  $C_p$ , as a function of the tip speed  $\lambda$  and pitch angle  $\beta$ . For low and medium wind speeds, the pitch angle is kept constant (in our case  $\beta = 0^\circ$ ) to allow the turbine to operate at its optimum condition. For high wind speeds, the pitch angle is increased to reject part of the aerodynamic power and keep the rotor speed within controllable limits. Fig. 5 shows the  $\lambda_{opt}$  corresponding to a pitch angle  $\beta$  of the blades. This scenario has been tested under variable speed conditions because, to maintain  $\lambda = \lambda_{opt}$ , it is necessary to vary the speed of the generator in response to wind speed variations.

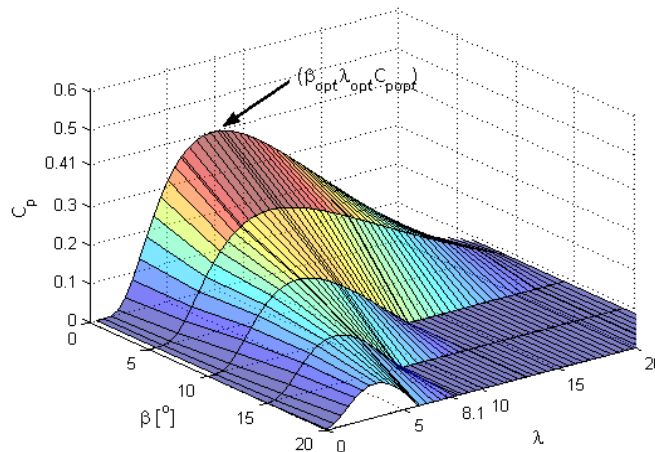


Fig. 5  $C_p(\beta, \lambda)$  for typical wind turbine with pitch control.

## 5. CONTROL OF THE GRID-SIDE CONVERTER

The formulation of standard  $H_\infty$  controller problem is depicted in Fig.6.

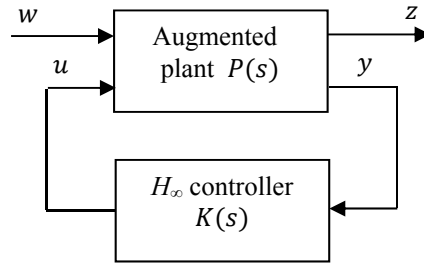


Fig. 6 General  $H_\infty$  problem.

Where  $w$  represents the disturbance signals,  $z$  are the errors to be minimized,  $y$  and  $u$  denote the outputs and control inputs respectively.  $P(s)$  represents the augmented plant transfer function matrix formed with the nominal plant transfer function and the weighting functions which reflect the design specification and  $K(s)$  is the controller transfer function.

The optimisation problem of Fig. 6 can be solved either using the algebraic riccati equation (ARE) [21] or by the LMI [22, 23] method which is presented next.

### 5.1. $H_\infty$ Design Based on LMI Technique

Consider the linear time invariant (LTI) system described by:

$$\begin{cases} \dot{x}(t) = Ax(t) + B_1w(t) + B_2u(t) \\ z(t) = C_1x(t) + D_{11}w(t) + D_{12}u(t) \\ y(t) = C_2x + D_{21}w(t) + D_{22}u(t) \end{cases} \quad (5)$$

Where  $x \in R^n$  is the state,  $w \in R^{mw}$  is the perturbation on the input,  $z \in R^{nz}$  is the controlled output,  $u \in R^{nu}$  is control law,  $y \in R^{ny}$  is the measured output and  $A, B_1, B_2, C_1, C_2, D_{11}, D_{12}, D_{21}$ , are constant matrices with appropriate sizes. Throughout the paper, it is assumed that:

H1) The system  $(A, B_2, C_2)$  is detectable and stabilizable.

H2)  $D_{22} = 0$ .

The controller  $K(s)$  stabilizes the system and satisfies:

$$\|\mathcal{F}(P, K)\|_\infty < \gamma \quad (6)$$

In  $H_\infty$  framework, LMI technique uses the following lemma (Bounded Real Lemma):

*Lemma 1:* Consider the system  $G(s)$  of equation (5). The following two conditions are equivalent:

- (i)  $\|G(s)\|_\infty < \gamma$  and  $A$  is stable.
- (ii) There exists a matrix  $X$ , symmetric and positive definite, that is solution of the following LMI:

$$\begin{bmatrix} A_f^T Q + Q A_f & Q B_f & C_f^T \\ B_f^T Q & -\gamma I_{nu} & D_f^T \\ C_f^T & D_f^T & -\gamma I_{ne} \end{bmatrix} < 0 \quad (7)$$

This result is known as the Kalman- Yacubovich -Popov lemma [24]. It easy to see that the set of solutions given by (7) form a convex set which can be solved using some optimization techniques [25-26]. The Bouded Real Lemma can be used to calculate the  $H_\infty$  norm of a linear system via the resolution of the following generalized eigenvalues problem: Find matrices  $Q = Q^T$  and  $R = R^T$  which minimise  $\gamma^2$ .

The regulator problem can be instantly solved using LMI toolbox instruction of Matlab [14].

The closed-loop system matrices are given by:

$$\left[ \begin{array}{c|c} A_f & B_f \\ \hline C_f & D_f \end{array} \right] = \left[ \begin{array}{cc|c} A + B_2 D_c C_2 & B_2 C_c & B_1 + B_2 D_c D_{21} \\ & B_c C_1 & A_c & B_c D_{21} \\ \hline C_1 + D_{12} D_c C_2 & D_{12} C_c & D_{11} + D_{12} D_c D_{21} \end{array} \right] \quad (8)$$

The feasibility of the standard  $H_\infty$  problem is tested by the following theorem:

*Theorem 1:* The  $H_\infty$  problem has a solution if there exist symmetric matrices  $X$  and  $Y$  that verify the following three LMI conditions:

$$\left[ \begin{array}{c|c} N_X & 0 \\ \hline 0 & I_{nw} \end{array} \right]^T \left[ \begin{array}{cc|c} AX + XA^T & XC_1^T & B_1 \\ & C_2 X & -\gamma I_{ne} & D_{21} \\ \hline B_1^T & D_{21}^T & -\gamma I_{nw} \end{array} \right] \left[ \begin{array}{c|c} N_X & 0 \\ \hline 0 & I_{nw} \end{array} \right] < 0 \quad (9)$$

$$\left[ \begin{array}{c|c} N_Y & 0 \\ \hline 0 & I_{ne} \end{array} \right]^T \left[ \begin{array}{cc|c} A^T Y + Y A & Y B_1 & C_1 \\ & B_1^T Y & -\gamma I_{nw} & D_{21}^T \\ \hline C_2 & D_{21} & -\gamma I_{ne} \end{array} \right] \left[ \begin{array}{c|c} N_Y & 0 \\ \hline 0 & I_{ne} \end{array} \right] < 0 \quad (10)$$

$$\left[ \begin{array}{c|c} X & I_n \\ \hline I_n & Y \end{array} \right] \geq 0 \quad (11)$$

Where  $N_X$  and  $N_Y$  are the kernel of matrices  $[C_2 \ D_{21}]$  and  $[B_2^T \ D_{12}^T]$  respectively.

The controller is determined according to the following steps:

1. Determine matrices  $X$  and  $Y$  using Theorem 1.
2. Let  $r$  be the rank of the  $(I_n - XY)$  matrix. Matrices  $M$  and  $N \in R^{n \times r}$  (i.e.  $M$  and  $N$  are full rank) are determined using singular value decomposition (SVD) as:

$$MN^T = I_n - XY \quad (12)$$

The Lyapunov matrix is then determined as:

$$Q = \begin{bmatrix} Y & N \\ N^T & -M^+ X N \end{bmatrix} \quad (13)$$

Where  $M^+$  denotes the pseudo-inverse of  $(M^+ M = I_r)$ .

Once the Lyapunov matrix is obtained, inequality (7) is then an LMI which provides the  $A_c, B_c, C_c, D_c$  solution matrices for the controller  $K(s)$ .

## 5.2. Augmented Plant Model

The augmented state space model  $P(s)$  of an LTI system is based on the weighting functions  $w_1(s), w_2(s)$ , and  $w_3(s)$  which correspond to the error, control and output signals respectively. The sub-optimal  $H_\infty$  problem solution is directly applicable to the mixte sensitivity problem and therefore to the loop shaping. Hence, only a minimal realization of the augmented system  $P(s)$  needs to be calculated.

The weighting functions  $w_i$  are obtained using the criterion of mixed sensitivity given by:

$$\left\| \begin{array}{c} w_1 S \\ w_2 K S \\ w_3 T \end{array} \right\|_\infty < 1 \quad (14)$$

The sensitivity function  $S$  and the additional sensitivity function  $T$  are used in the synthesis of the controller and are given by:

$$\begin{cases} S = (I + GK)^{-1} \\ T = GK(I + GK)^{-1} \end{cases} \quad (15)$$

The augmented plant model  $P$  is built from the nominal model  $G$ , which is derived in Appendix C and weighting matrices  $w_i$  as follows:

$$P = \left[ \begin{array}{c|c} w_1 & -w_1 G \\ \hline 0 & w_2 \\ 0 & w_3 G \\ \hline I & -G \end{array} \right] = \begin{bmatrix} A & B_1 & B_2 \\ C_1 & D_{11} & D_{12} \\ C_2 & D_{21} & D_{22} \end{bmatrix} \quad (16)$$

Fig. 7 depicts a block diagram of the equivalent  $H_\infty$  problem based on the criterion  $\left\| \begin{bmatrix} w_1 S \\ w_2 K S \\ w_3 T \end{bmatrix} \right\|_\infty < 1$ .

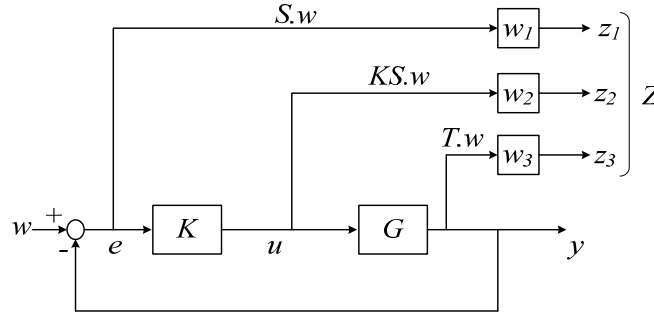


Fig. 7 Mixed sensitivity problem.

The error  $e$ , control  $u$  and output signals are weighted by filters  $w_1(s)$ ,  $w_2(s)$  and  $w_3(s)$  respectively which are calculated for the various disturbances on the input,  $b(t)$ , output,  $d(t)$  and measurement noise  $\eta(t)$  respectively as shown in Fig. 8. Here, the measurement noise  $\eta(t)$  is assumed to be zero.

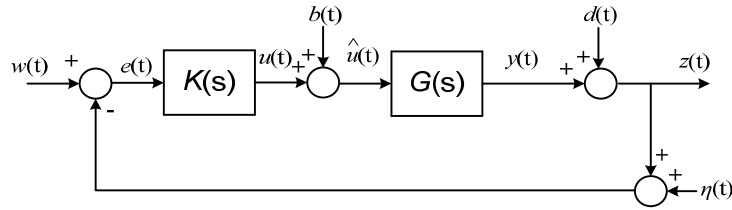


Fig. 8 Typical feedback control system with disturbances acting on the input, output and measurement.

Where:  $K(s)$  is the controller transfer function,  $G(s)$  is transfer function system to be controlled,  $b(t)$ ,  $d(t)$  and  $\eta(t)$  are the disturbances acting on the system.

In our case, for instance an asymmetrical fault created at the grid side is considered as a perturbation to the input of the system (i.e.  $b(t)$ ) and changes in wind speed are considered as a disturbance acting on the output of the system (i.e.  $d(t)$ ). The measurement noise  $\eta(t)$  is not considered in this study.

The output transfer function is:

$$Z(s) = \begin{bmatrix} z_1 \\ z_2 \\ z_3 \end{bmatrix} = \begin{bmatrix} w_1 S \\ w_2 K S \\ w_3 T \end{bmatrix} w(s) \quad (17)$$

One recognises a perturbation problem where the effects of  $w$  on the filtered outputs ( $z_1$ ,  $z_2$ ,  $z_3$ ) must be reduced below a ratio of one.

There are no general formulas for the formulation of weighting functions that will work in all cases. In our case, usual performance specifications require the sensitivity function to be small at low frequency and to be able to stabilize  $|S|_\infty = 1 = 0 \text{ dB}$  at high frequency as shown in Fig. 9 [27, 28].

The reference tracking performance of the controller is related to the magnitude plot of the sensitivity function  $S(j\omega)$  which has a slope of +40 dB/dec at low frequencies. Hence the closed loop system is able to track the

reference signals in the form of steps with zero steady-state errors. The magnitude  $|S(j\omega)|$  cuts the 0 dB axis at  $\omega = 10^3$  rad/sec. Therefore, the 5% settling time will be in the order of  $\frac{3}{1000} = 3$  msec.

The input disturbance rejection characteristic of the control system can be examined by looking at the magnitude plot of the transfer function that links the disturbance  $b(t)$  to the tracking error trajectory of  $GS$ .

As a result, the closed-loop system is able to reject step-like disturbances. By examining the curve, the frequency range over which the magnitude is the largest provides an indication on how much the output is affected by the disturbance and the time of rejection of the disturbance.

On the other hand, the magnitudes plots of the transfer functions  $KS$  and  $T$  indicate that they have low pass characteristic, which would attenuate the effect of noise on the control signal ( $KS$  connects the noise  $\eta(t)$  to the control  $u(t)$ ) and on the output of system ( $T$  connects the noise  $\eta(t)$  the output  $y(t)$ ). In addition, the peak of the magnitude plot of  $T$  provides an estimate of the overshoot of the closed-loop step response.

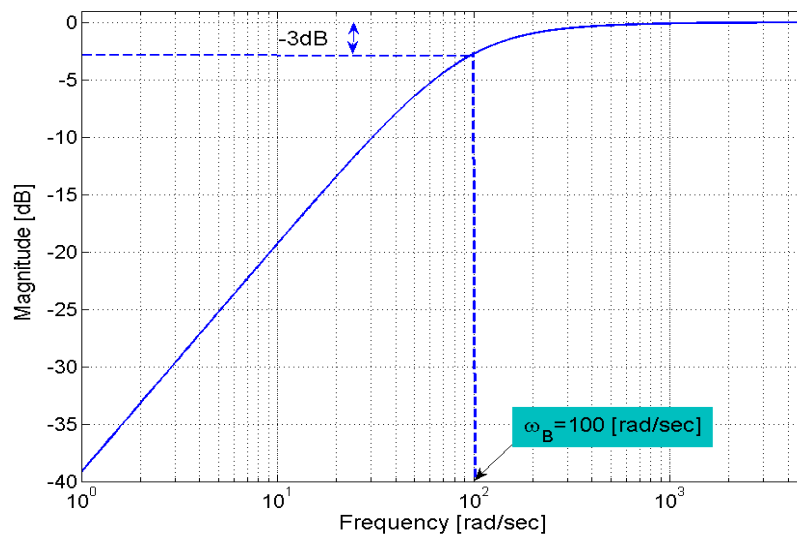


Fig. 9 Bode diagram of the sensitivity function.

For multi-input multi-output (MIMO) problems, the weighting functions  $w_1(s)$ ,  $w_2(s)$ , and  $w_3(s)$  can be selected as diagonal matrices [29].

$$w_1 = w_S I_3 \quad w_2 = \mu I_2 \quad w_3 = w_T I_3 \quad (18)$$

Where  $w_S$  represents the filter associated to the sensitivity function  $S$ ,  $\mu$  is a positive real number chosen as a constant (in our case  $\mu = 1$ ),  $w_T$  is a filter corresponding to the complementary sensitivity function  $T$  and  $I_m$  are  $(m \times m)$  identity matrices.

The passband  $\omega_B$  of the filter  $w_S(s)$  is obtained from Bode diagram of the sensitivity function at  $-3$  dB. For the system considered in this study, the value of the passband is  $\omega_B = 100$  rad/sec (see Fig. 8).

In order to improve the accuracy of the control system, the sensitivity function gain  $S_0$  of  $S$  is chosen small at low frequency.

Furthermore, the  $w_S(s)$  filter was chosen so that the Bode diagram of  $\gamma_{opt}/w_S(j\omega)$  cuts the 0 dB axis at 100 rad/sec (passband) and has a sufficiently small gain at low frequency.

Finally, the  $w_S(s)$  filter is calculated based on the sensitivity function  $S$  values at low frequency ( $S_0$ ) and high frequency  $S_\infty$  ( $S_\infty = 0$  dB) and the passband  $\omega_{B1}$  by:

$$w_S^{-1} = \frac{s + S_0 \omega_B}{\frac{s}{s_\infty} + \omega_B} = \frac{s + 0.078}{s + 100} \quad (19)$$

Fig. 10 shows the Bode diagram of the singular values of  $\frac{\gamma_{opt}}{w_S(j\omega)}$  when  $\gamma_{opt} \approx 1.42$  (corresponding to the passband  $\omega_B$ ).

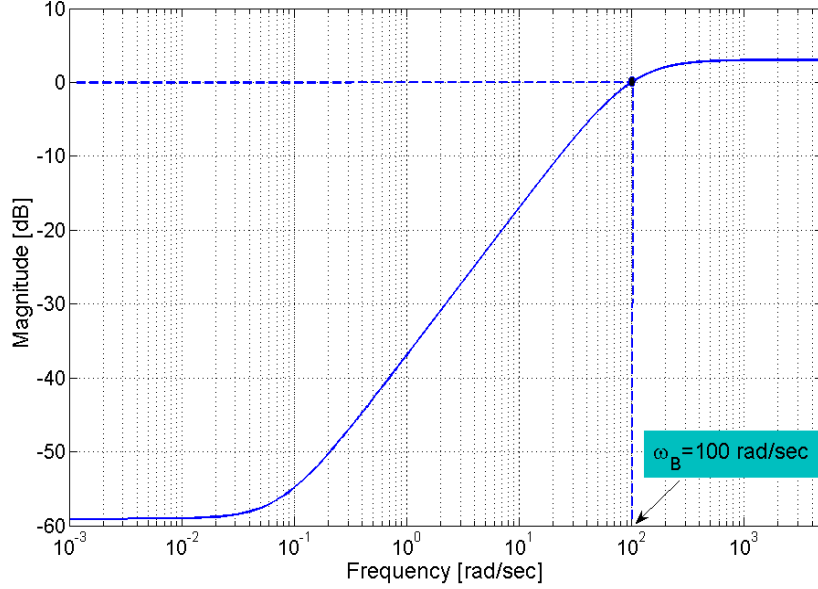


Fig. 10 Bode diagram of the singular value of  $\gamma_{opt}/w_S(j\omega)$ .

The filter transfer function  $w_T(s)$  can be calculated using an additional sensitivity function  $T$ . For the same passband  $\omega_B$ , a low frequency amplitude of 0 dB at  $T_0 = 1$  and a high-frequency amplitude of  $-100$  dB set at  $T_\infty = 10^{-5}$ , the filter transfer function  $w_T(s)$  is determined by:

$$w_T^{-1} = \frac{T_\infty s + \omega_B}{s + \frac{\omega_B}{T_0}} = \frac{10^{-5}s + 100}{s + 100} \quad (20)$$

Fig. 11 shows the Bode diagram of the singular value of  $\frac{\gamma_{opt}}{w_T(j\omega)}$  :

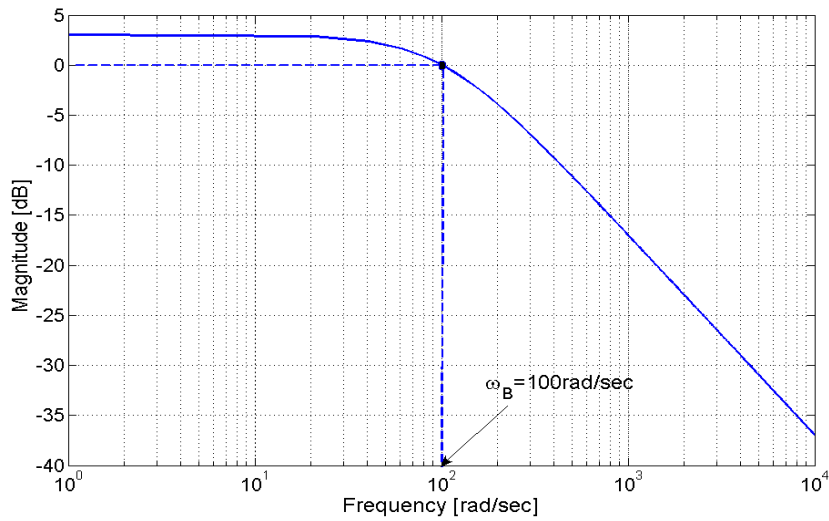


Fig. 11 Bode diagram of the singular value of  $\gamma_{opt}/w_T(j\omega)$ .

The order of the augmented system  $P(s)$  is the sum of the degrees of  $G(s)$  and different weight functions:

$$\text{deg}(P) = \text{deg}(G) + \text{deg}(w_1) + \text{deg}(w_2) + \text{deg}(w_3) \quad (21)$$

The controller  $K(s)$  in state-space is written as:

$$\begin{cases} \dot{x}_c(t) = A_c x_c(t) + B_c y(t) \\ u(t) = C_c x_c(t) + D_c y(t) \end{cases} \quad (22)$$

$x_c$  and  $A_c, B_c, C_c$ , et  $D_c$  denote the state vector and the state, input and output matrices of the  $H_\infty$  controller which are given by:

$$A_c = \begin{bmatrix} -1580.85 & -19.91 & -0.0315 & 0 & -0.0033 & 0.00103 & 0 & 0.00027 \\ -48.70 & -2543.22 & -0.0033 & 0 & 0.0315 & 0 & -0.0014 & -0.0023 \\ 0 & 0 & -0.013 & 0 & 0 & 0 & 0 & 0 \\ 0 & 0 & 0 & -0.013 & 0 & 0 & 0 & 0 \\ 0 & 0 & 0 & 0 & -0.013 & 0 & 0 & 0 \\ -1.305 \times 10^9 & 2.3 \times 10^6 & 3624.2 & 0.00021 & 382.56 & -1149.4 & -304.03 & -30.78 \\ -1.1807 \times 10^7 & 2.515 \times 10^9 & -805.52 & 0.0041 & 7628.713 & 298.43 & -1364.052 & -806.64 \\ 0 & 0 & 0 & 0 & 0 & 0 & 0 & 81.65 & 0 \end{bmatrix}$$

$$B_c = \begin{bmatrix} 0 & 0 & 0 \\ 0 & 0 & 0 \\ 308.41 & 0 & 0 \\ 0 & 308.41 & 0 \\ 0 & 0 & 308.41 \\ 0 & 0 & 0 \\ 0 & 0 & 0 \\ 0 & 0 & 0 \end{bmatrix}, \quad D_c = \begin{bmatrix} 0 & 0 & 0 \\ 0 & 0 & 0 \end{bmatrix} \quad (23)$$

$$C_c = \begin{bmatrix} 1470.07 & -2.6 & -0.004 & 0 & -0.00043 & 0.00013 & -1.14 \times 10^{-5} & 3.47 \times 10^{-5} \\ -6.32 & 1345.25 & -0.00043 & 2.2 & 0.004 & 0 & -0.00018 & -0.0003 \end{bmatrix}$$

In the case where the controller  $K(s)$  is strictly proper (i.e.  $D_c = 0$ ) and its order is equal to that of the augmented system  $P(s)$ , this type of controller is termed *central compensator* and has the following structure:

The controller transfer function matrix is:

$$K(s) = \frac{u(t)}{y(t)} = [C_c [sI - A_c]^{-1} B_c + D_c] \quad (24)$$

$$K(s) = \begin{bmatrix} k_1(s) & 0 \\ 0 & k_2(s) \end{bmatrix} \quad (25)$$

With:

$$\begin{cases} k_1(s) = \frac{-7.15 \times 10^{-8} (s + 1.3 \times 10^4) (s + 2502) (s^2 + 0.026s + 1.67 \times 10^{-3}) (s^2 + 2826s + 7.947 \times 10^6)}{(s + 97.23) (s + 0.01292)^3 (s^2 + 2766s + 3.163 \times 10^6) (s^2 + 3774s + 6.682 \times 10^6)} \\ k_2(s) = \frac{6.77 \times 10^{-7} (s + 1.3 \times 10^4) (s + 980.7) (s + 20) (s + 0.01292)^2 (s^2 + 2764s + 3.304 \times 10^6)}{(s + 97.23) (s + 0.01292)^3 (s^2 + 2766s + 3.163 \times 10^6) (s^2 + 3774s + 6.682 \times 10^6)} \end{cases}$$

### 5.3. Determination of the Rotating Reference Frame

The Park transformation used for the grid side quantities is based on the reference frame related to the rotating field of the grid, the d-axis is aligned with the source voltage vector. Thus the q-axis voltage is zero ( $v_q = 0$ ). In this case, the active power on the grid side is given by:

$$P = \frac{3}{2} v_d i_d \quad (26)$$

If the power losses are neglected, then  $P$  is equal to the reference power  $P_{MPPT}$  obtained via the MPPT strategy based on the characteristic of the wind turbine given in Fig. 12 which has been implemented in a form of look-up table.

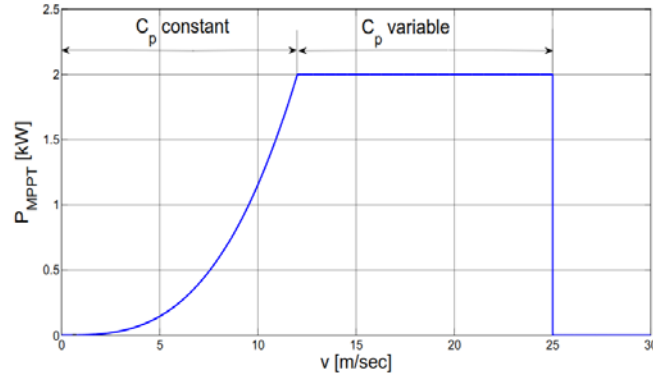


Fig. 12 Power curve of a typical wind turbine.

In the first interval, with wind speeds between 3 and 12 m/sec, the variable speed operation is used to maximize generator power depending on the wind speed available. In this region, the blade pitch angle is kept at its optimal value  $\beta = 0^\circ$ . For wind speeds over 12 m/sec and less than 25 m/sec, the blade pitch system is used to maintain the power of the generator at its nominal value. Finally, for wind speeds greater than 25m/sec, the pitch angle should be maintained at its maximum value  $\beta = \beta_{max}$  in order to protect the wind turbine.

Indeed, given the wind forces to which the blades may be subjected, it is important to limit the rate of change of the pitch angle. Appropriate values are about 10 °/s during normal operation and 20 °/s in the case of emergency [30].

The d-axis voltage  $v_d$  is given by (if the q-axis voltage is zero):

$$v_d = \sqrt{\frac{2}{3}} V_s \quad (27)$$

Substituting equation (26) into (27), the d-axis current reference is calculated as:

$$i_{dref} = \sqrt{\frac{2}{3}} \frac{P_{ref}}{V_s} \quad (28)$$

The  $H_\infty$  controller output signals are the inverter conversion ratio ( $D$ ) and the phase  $\delta$  i.e.  $u = [\delta_\Delta D_\Delta]^T$ .

$D$  is defined as the ratio between the fundamental of the output voltage ( $v_o$ ) and the DC voltage ( $v_{dc}$ ).

The grid-side inverter voltage amplitude is obtained by:

$$|v_o| = \sqrt{v_{od}^2 + v_{oq}^2} = D v_{dc} \quad (29)$$

Using the two control laws and equation (29), the grid-side inverter voltages after Park transformation are given by:

$$\begin{cases} v_{od} = |v_o| \cos \delta = D v_{dc} \cos \delta \\ v_{oq} = |v_o| \sin \delta = D v_{dc} \sin \delta \end{cases} \quad (30)$$

The inverse Park transformation is applied to equations (30) to find the three-phase voltages  $v_{oabc}$ . Then, using the transformation of Concordia:

$$\begin{bmatrix} v_{o\alpha} \\ v_{o\beta} \end{bmatrix} = \sqrt{\frac{2}{3}} \begin{bmatrix} 1 & -1/2 & -1/2 \\ 0 & \sqrt{3}/2 & -\sqrt{3}/2 \end{bmatrix} \begin{bmatrix} v_{oa} \\ v_{ob} \\ v_{oc} \end{bmatrix} \quad (31)$$

Fig. 13 illustrates the switching control strategy of the three-level inverter based on multivariable  $H_\infty$  control.

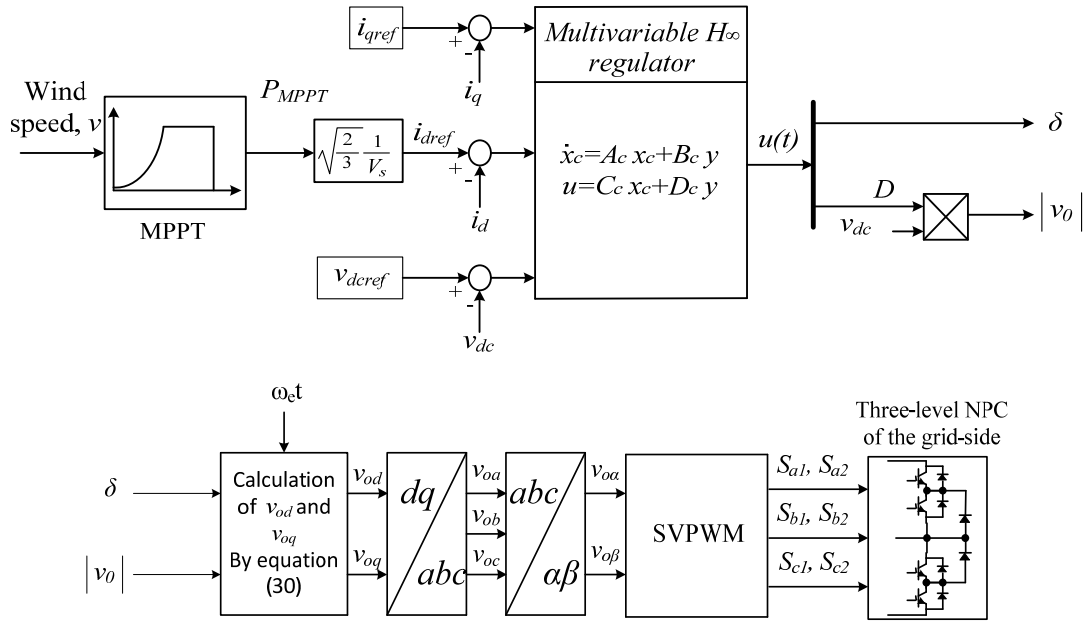


Fig. 13 Multivariable  $H_\infty$  control of the a three-level grid-side inverter.

## 6. SIMULATION RESULTS

The simulation model is implemented in Simulink/SimPowerSystems with the parameters listed in Appendix C. The proposed control system is tested under different operating conditions of the WECS. Two simulation scenarios are performed to evaluate the dynamic behaviour of the system under variable and stochastic wind speed characteristics and under asymmetric dip voltage in the grid simulated as a 20% voltage decrease and lasting for 300 ms. The single-phase fault occurs between  $t = 1$  s and  $t = 1.3$  s .

A simulation study to compare the proposed  $H_\infty$  based control strategy with a classical PI controller with respect to power quality is also presented.

### A. Simulation of the system under variable wind speed conditions

In Fig. 14 are shown the responses of the real and reactive powers of the grid. The references are provided by the MPPT block. Initially, before the turbine starts rotating, the real power shown on the plot corresponds to the constant power losses of the generator.

At  $t = 0.5$  sec, the turbine is started with a wind speed of  $v = 10$  m/sec, the generator is then driven by a mechanical torque  $T_t = -11$  Nm and delivers an output power  $P_g = -1.2$  kW to the grid.

After the wind turbine begins to generate the rated torque ( $T_t = -16$  Nm), the generator starts to deliver a nominal power  $P_g = -2$  kW to the grid.

The responses of rotor speed, the mechanical torque produced by the turbine with the electromagnetic torque of the generator, the tip speed ratio  $\lambda$  and the power coefficient  $C_p$  are shown in Fig. 15. The generator is driven at a speed  $N_r = 1335$  rpm when the electromagnetic torque is equal to  $-11$  Nm and at 1600 rpm, when the torque is  $-16$  Nm. The power coefficient  $C_p$  is zero before the turbine starts and reaches its maximum value of 0.41 after starting the turbine. Similarly, the tip speed reaches a maximum value of  $\lambda = 8.1$ .

Fig. 16 shows the form of the DC link voltage  $v_{dc}$ , the active ( $i_d$ ) and reactive ( $i_q$ ) currents and phase “a” current waveforms, for the generator and grid respectively. Note that the DC link voltage  $v_{dc}$  follows its reference value set to 800V.

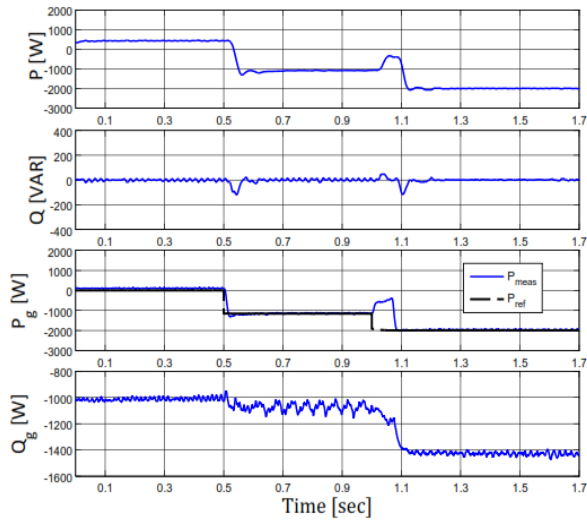


Fig. 14 Real and reactive powers of the generator and grid and.

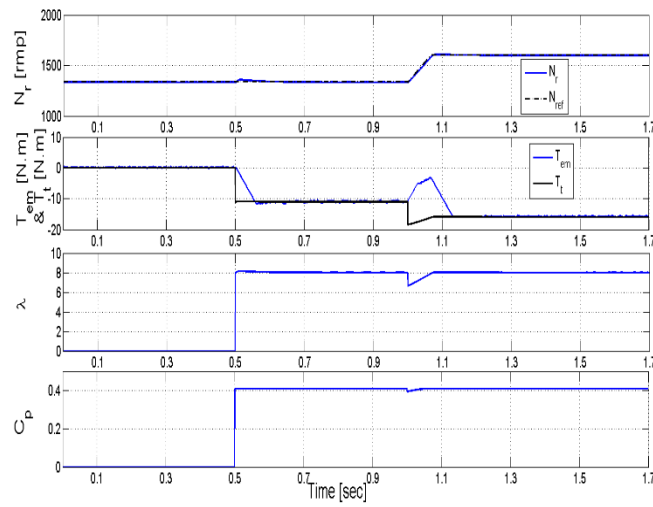


Fig. 15 Responses of the generator rotor speed, electromagnetic and mechanical torque, tip speed ratio  $\lambda$  and power coefficient  $C_p$ .

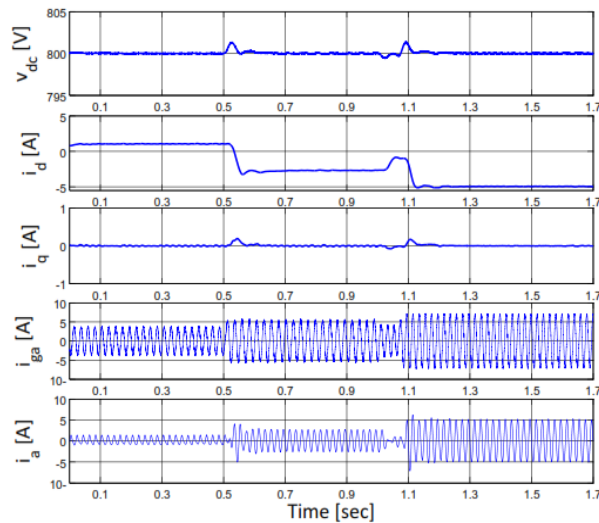


Fig. 16 Responses of the DC link voltage, grid currents  $i_d$  and  $i_q$ , phase "a" current of the generator ( $i_{ga}$ ) and the grid ( $i_a$ ).

Fig.17 shows the grid-side inverter voltages ( $v_{od}$ ,  $v_{oq}$ ) and the  $H_\infty$  controller outputs ( $D$ ,  $\delta$ ). The inverter conversion ratio  $D$  controls the DC voltage and the active part of the current  $i_d$  and the phase angle  $\delta$  controls the flow of the reactive current  $i_q$ . The phase angle  $\delta$  should reach a low steady-state value to ensure that the reactive power flow between the grid and the converter is zero (i.e. power factor is zero).

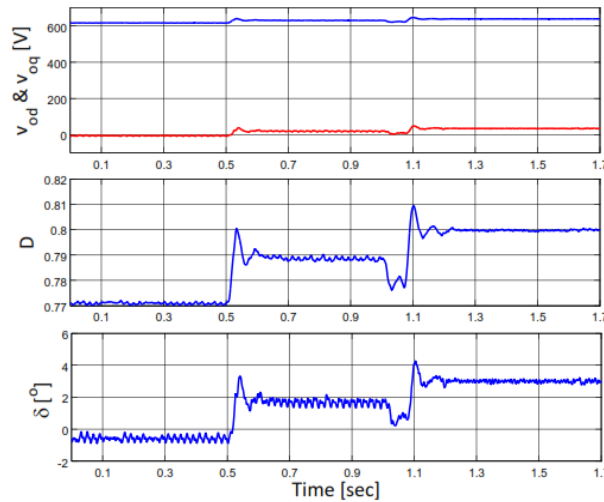


Fig. 17 Responses of the grid-side inverter voltages and control inputs.

The tracking performance of the proposed control scheme has correspondingly been tested under more realistic conditions with stochastic and fluctuating wind speed characteristics. In the simulation results of Fig. 18 throughout Fig. 22, two situations have been considered:

*Case 1:* During the interval  $2 \leq t \leq 6$  s, there is an acceleration of wind speed ( $v \geq 12$  m/s) and this corresponds to the zone of aerodynamic protection or pitch control. From Fig. 18, it can be seen that the power is kept at -2 kW (rated power of the generator). The speed and torque of the generator are maintained to their rated values in order to protect the wind turbine against overspeed of the wind as shown in Fig. 19. The power coefficient  $C_p$ , the rate after  $\lambda$ , the pitch angle  $\beta$  are varied to reject Fig. 22 excess of power.

*Case 2:* For all other  $t$ , the wind speed is  $v \leq 12$  m/s and this corresponds to the zone of MPPT operation to extract the maximum power. Fig. 18 shows that the power varies according to the wind speed variations. The speed and torque of the generator, on the other hand, are varied in order to maximize the power available from the wind (Fig. 19). As shown in Fig. 22, in this case the power coefficient  $C_p$ , the rate after  $\lambda$ , the pitch angle  $\beta$  are maintained constant.

The DC voltage  $v_{dc}$ , the currents  $i_d$  and  $i_q$  are shown in Fig. 20 and the  $H_\infty$  controller outputs ( $D$ ,  $\delta$ ) are given in Fig. 21. It can be noticed that  $v_{dc}$  is regulated to its reference value of 800 V but exhibiting fluctuations in the MPPT control zone. Similar remark applies to the currents  $i_d$  and  $i_q$  and the controller outputs ( $D$ ,  $\delta$ ).

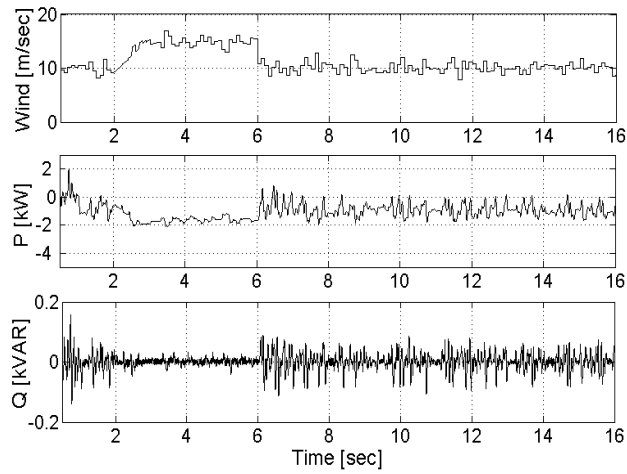


Fig. 18 Wind speed and the grid real and reactive powers.

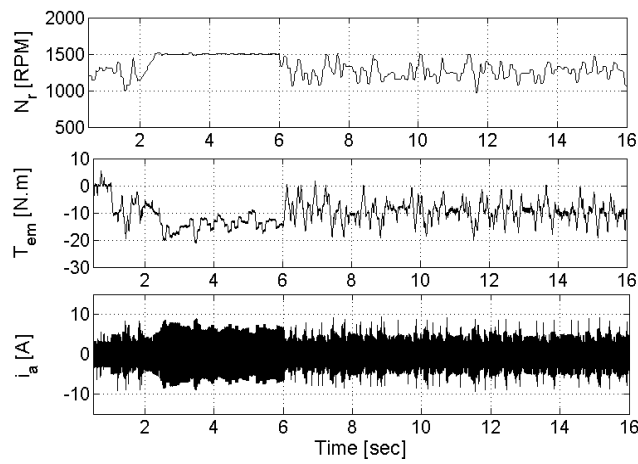


Fig. 19 Generator rotor speed and torque and grid current (Phase “a”).

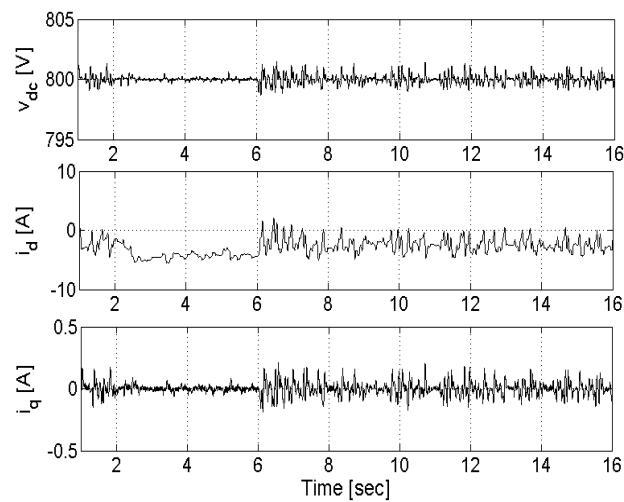


Fig. 20 Waveforms of the DC voltage, d- and q-axis grid currents.

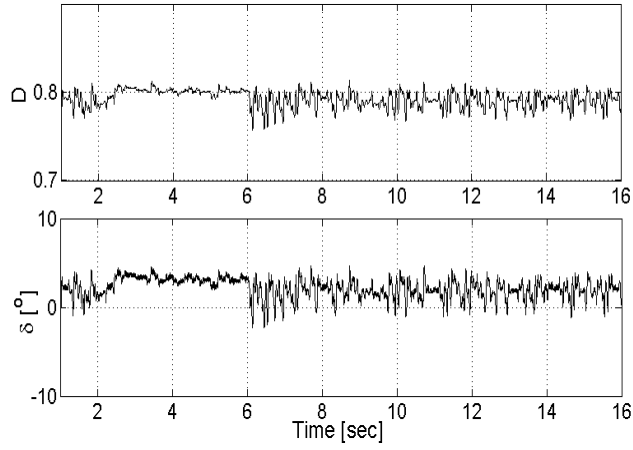


Fig. 21  $H_\infty$  controller output signals  $\delta$  and  $D$ .

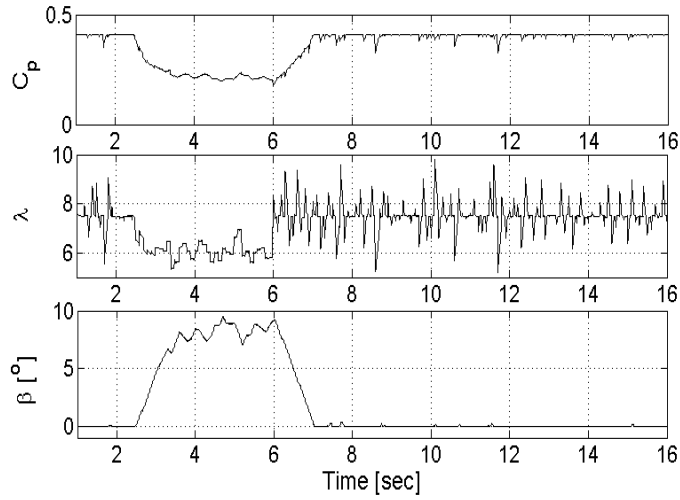


Fig. 22 Power coefficient, tip speed ratio and the orientation angle of the blades.

The designed  $H_\infty$  controller is compared with a PI controller under stochastic wind speed conditions. As shown in Fig. 23, the turbulence component of the wind speed is simulated as a stationary random process and therefore does not depend on the mean value of the wind speed. The simulation results are shown in Fig. 23 and Fig. 24. From these results, it can be noticed that the proposed  $H_\infty$  controller over-performs the PI controller and provides better transient response characteristics under these more realistic wind speed conditions. Only few ripples in the transient responses of the real and reactive powers (Fig. 23) and grid-side currents (Fig. 24) in the case of  $H_\infty$  controller. There is also an improvement in the response of the DC link voltage in the case of  $H_\infty$  controller.

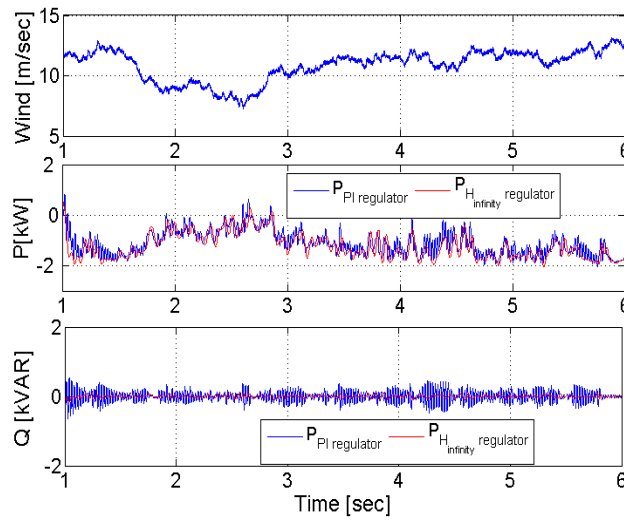


Fig. 23 Response of the wind speed, the active and reactive power of the grid.

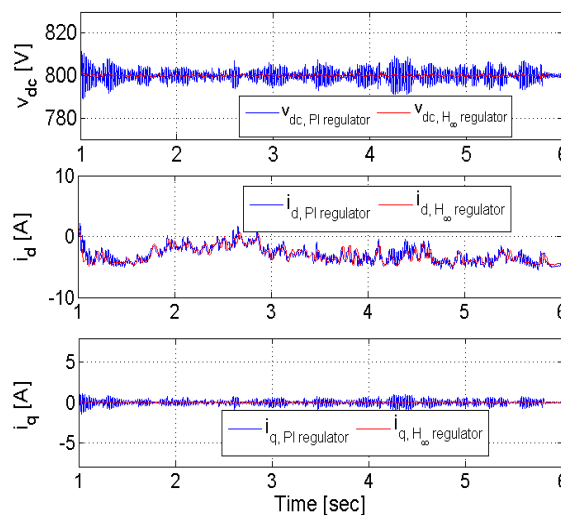


Fig. 24 Response of the DC voltage, the active and reactive currents of the grid.

In Fig. 25, two wind speed conditions are considered:

- $v \leq 12$  m/s, the system operates in the region of maximum power (MPPT control). In this case  $C_p$ ,  $\lambda$  and  $\beta$  assume optimal values 0.41, 8.1 and  $0^\circ$  respectively and are constant.
- $v > 12$  m/s, pitch control is enabled to protect the system and maintains the power of generator at its rated value.

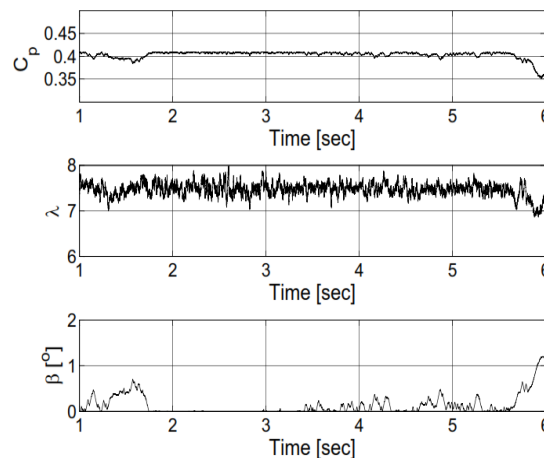


Fig. 25 Power factor coefficient, tip speed ratio and orientation angle of the blade.

*B. Simulation of the system under asymmetric fault conditions*

A single-phase fault has been simulated as a decrease of 20% of phase “a” voltage peak value. The fault condition has been applied to the system under PI control and the proposed  $H_\infty$  controller.

Fig. 26 shows the responses of the grid voltage (phase “a”), the DC link, real and reactive powers of the grid.

The application of the fault, caused a small drop in power and there was no effect on both the DC link voltage and reactive power of the grid. In the case of PI controller, some oscillations can be noticed in the voltage and also in the real and reactive powers of the grid after the application of the single-phase fault.

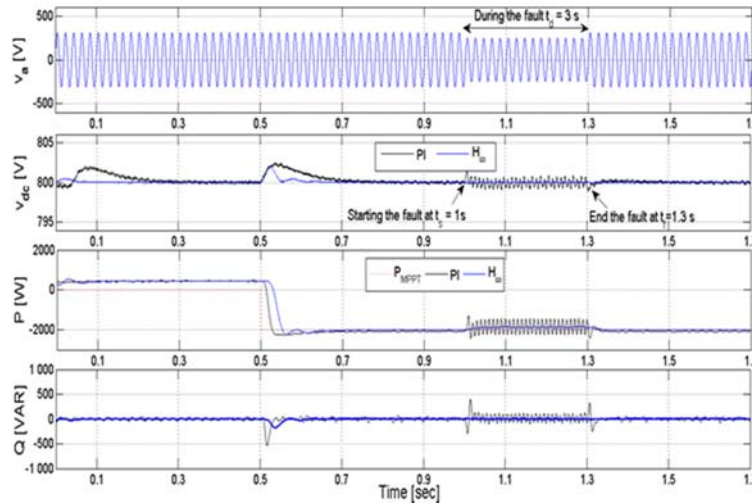


Fig. 26 Waveforms of phase “a” grid voltage, DC link voltage, grid real and reactive powers with a single-phase fault.

*C. FFT based power quality analysis*

Fig. 27 shows phase “a” grid current with PI and  $H_\infty$  controllers respectively and the associated harmonic spectra. The THDs obtained with the PI and  $H_\infty$  multivariable controllers are 1.51% and 0.38% respectively. The lowest THD is achieved with the  $H_\infty$  multivariable controller. Note that in this case, the harmonics component can be moved away from the fundamental frequency. This information is advantageous for the design of an appropriate filter to achieve high-quality currents at the output of the inverter.

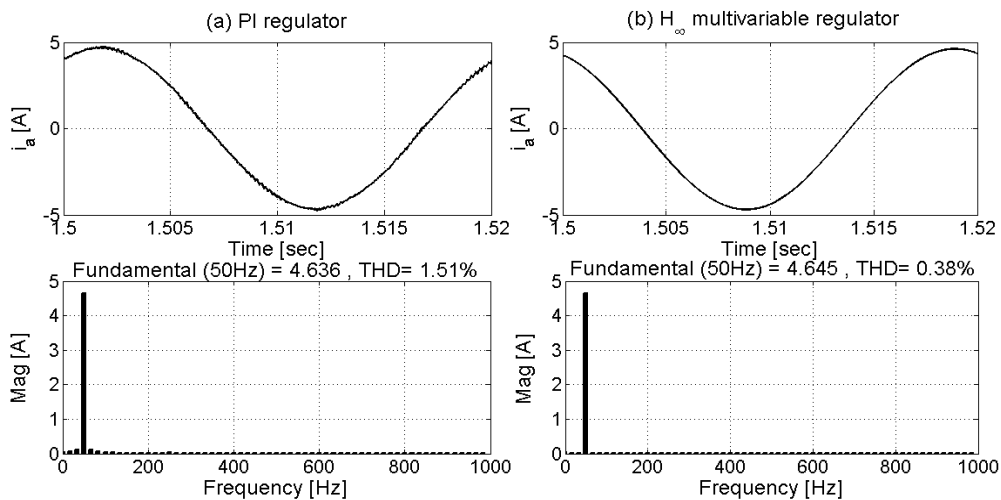


Fig. 27 Grid phase “a” current and its harmonic spectrum (a) PI control (b)  $H_\infty$  control

D. Simulation of the system under variable parameters condition: Comparison between  $H_\infty$  controller and PI controller

A comparative study is performed between  $H_\infty$  controller and PI controller under variable parameters conditions for a wind speed  $v = 12$  m/sec. The grid side resistance  $R_f$  is varied by 10% and 15% and Fig. 28 shows the real and reactive power of the network for these two cases respectively. From these results, one can notice that, for the classical PI controller, the generator provides -2 kW active power for  $R_f = 3.4 \Omega$  resistance. After the resistance value is varied (increases of 10 and 15%), the controller is unable to track the reference and a power loss is noted for both cases.  $H_\infty$ , however, demonstrates a better control and is able to adapt to this parameter variations of the system as shown in Fig. 28. It may be noted the active power follows its reference -2 kW at time  $t = 1.8$  sec despite changes in resistance grid side of the transformer.

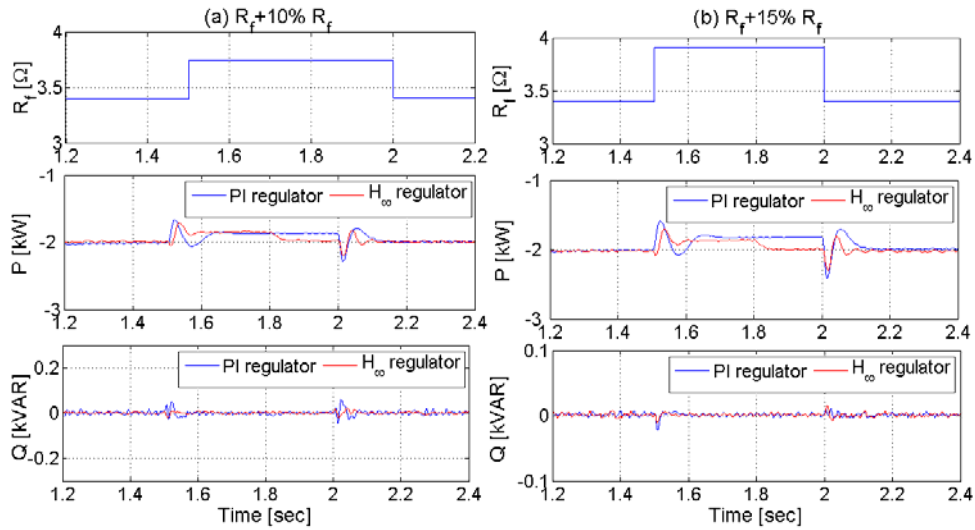


Fig. 28 Real and reactive power of the network:

(a) 10% increase in the grid resistance, (b) 15% increase in the grid resistance.

Fig. 29 shows the simulation results of the voltage  $v_{dc}$ ,  $D$  the ratio of conversion and the phase shift  $\delta$  to increase a 10% (a) and 15% (b) increase in the resistance. From these results it can be seen both  $H_\infty$  and PI controllers achieved good control of  $v_{dc}$  to its desired reference 800 V. The response is however faster in the case of  $H_\infty$ .

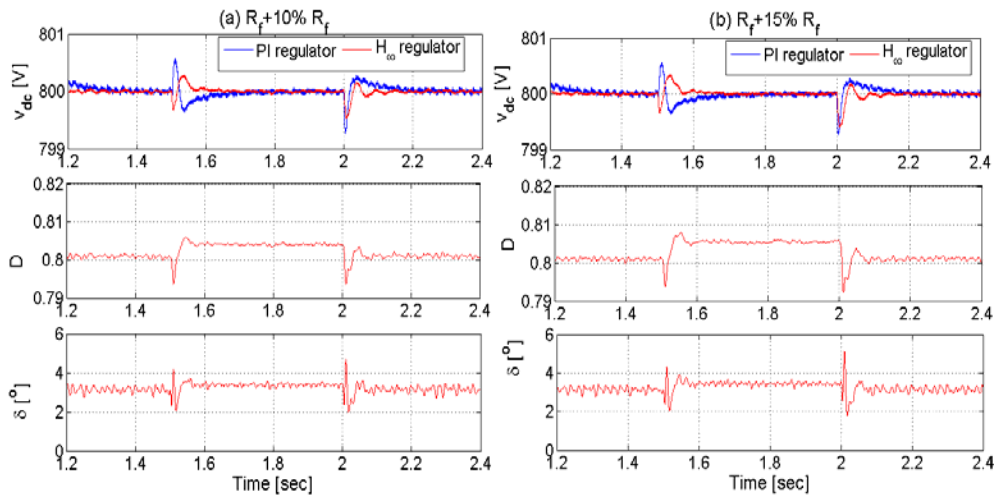


Fig. 29 DC voltage and  $H_\infty$  controller outputs:

(a) 10% increase in the grid resistance.

(b) 15% increase in the grid resistance.

## 5. Conclusions

This paper proposed a multivariable control scheme of a variable-speed WECS to improve the performance, stability and enhance the quality of the power delivered to the grid. The aim was to simulate and analyse a number of common problems that may affect the power grid including voltage dips, imbalance of the three-phase system, voltage fluctuations (or flickers) and harmonics.

The SCIG is controlled by DTC based on a three-level converter. The control signals for the generator-side and grid-side converters are obtained by the SVPWM method. The generator reference speed is obtained from a MPPT control algorithm. A multivariable  $H_\infty$  is designed using the LMI approach to simultaneously control the DC bus voltage and grid current. The reference for the direct component of the grid current is derived from reference power calculated by the MPPT strategy. The q-axis component of the grid current was used to control the flow of reactive power. To achieve a unity power factor in the system, the reference of the reactive power has been set to zero.

The paper presented a series of simulation results to show the performance and robustness of the proposed control approach under various operating conditions of the WECS including variable wind speed conditions and under asymmetric single phase fault in the grid. The simulation results with asymmetrical faults on the grid side demonstrate a superior dynamic performance, robustness and stability with the use of  $H_\infty$  control strategy as compared to the PI controller.

Finally, a comparative study between a classical PI control and the proposed  $H_\infty$ -based control strategy in terms of power quality is presented.

Overall, the proposed control scheme demonstrated good performance for all the simulation scenarios considered. A real-time implementation and validation of the proposed control approach is being considered using a wind turbine emulator setup.

## APPENDIX A: Model of the grid-side

Fig. A.1 shows the grid-side inverter with DC source. To achieve bidirectional current flow through the converter, every switch is accompanied by an antiparallel diode. The switched converter in normal operation produces current through neutral point  $N$ , for different characteristics, depending on the operating conditions. This current flow creates an unbalance (charge and discharge of the DC side of capacitors) in the DC voltage to every capacitance capacitor  $C_{dc}$ . Usually with a finite value capacitors, the converter requires a special modulation algorithm that achieves a balanced DC side voltage [31].

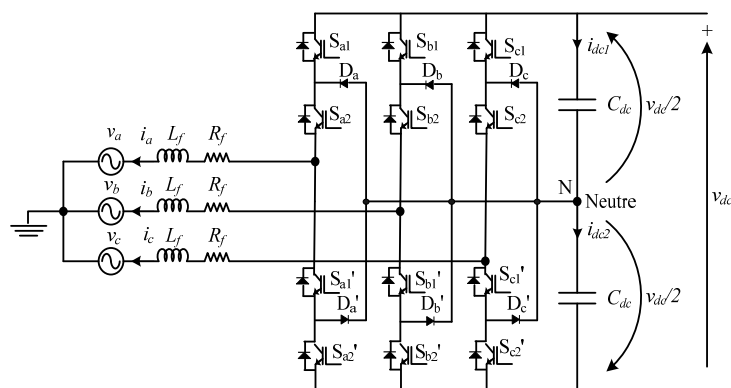


Fig. A.1 Three-level inverter with NPC ( $C_{dc} = 500 \mu\text{F}$ ).

This model is based on following simplifying assumptions [32-36]:

- ✓ All switches are supposed ideal.
- ✓ The three alternative source of voltages are balanced.
- ✓ The harmonics due the opening and closing actions of the switches are negligible.
- ✓ All voltage dips on the source side of inverter are represented by the resistor  $R_f$ .
- ✓ The currents and voltages in the capacitors are equal.

Using matrix representation, the three-phase abc system model of the network grid side is given by the following system of equations:

$$\frac{d}{dt} \begin{bmatrix} i_a \\ i_b \\ i_c \end{bmatrix} = \begin{bmatrix} \frac{R_f}{L_f} & 0 & 0 \\ 0 & \frac{R_f}{L_f} & 0 \\ 0 & 0 & \frac{R_f}{L_f} \end{bmatrix} \begin{bmatrix} i_a \\ i_b \\ i_c \end{bmatrix} + \frac{1}{L_f} \begin{bmatrix} v_a - v_{oa} \\ v_b - v_{ob} \\ v_c - v_{oc} \end{bmatrix} \quad (\text{A. 1})$$

From the second hypothesis, the voltages of the three-phase source are:

$$v_{abc} = \begin{bmatrix} v_a \\ v_b \\ v_c \end{bmatrix} = \sqrt{\frac{2}{3}} V_s \begin{bmatrix} \sin(\omega_e t + \delta) \\ \sin\left(\omega_e t - \frac{2\pi}{3} + \delta\right) \\ \sin\left(\omega_e t + \frac{2\pi}{3} + \delta\right) \end{bmatrix} \quad (\text{A. 2})$$

Where:

$V_s$  is the efficient phase voltage of the source.

$\delta$  is the phase angle between the fundamental voltages of the source and the inverter output voltages.

The Park transformation of equation (A.2) is given by:

$$v_{q,d,o} = V_s \begin{bmatrix} -\sin \delta \\ \cos \delta \\ 0 \end{bmatrix} \quad (\text{A. 3})$$

The system is balanced, so the homopolar part is zero. The model becomes:

$$\begin{bmatrix} v_q \\ v_d \end{bmatrix} = \begin{bmatrix} R_f & \omega_e L_f \\ -\omega_e L_f & R_f \end{bmatrix} \begin{bmatrix} i_q \\ i_d \end{bmatrix} + L_f \frac{d}{dt} \begin{bmatrix} i_q \\ i_d \end{bmatrix} + \begin{bmatrix} v_{oq} \\ v_{od} \end{bmatrix} \quad (\text{A. 4})$$

From equation (A.4), the model of the source-side currents is given by:

$$\frac{d}{dt} \begin{bmatrix} i_q \\ i_d \end{bmatrix} = \begin{bmatrix} -\frac{R_f}{L_f} & -\omega_e \\ \omega_e & -\frac{R_f}{L_f} \end{bmatrix} \begin{bmatrix} i_q \\ i_d \end{bmatrix} + \frac{1}{L_f} \begin{bmatrix} v_q - v_{oq} \\ v_d - v_{od} \end{bmatrix} \quad (\text{A. 5})$$

From the third hypothesis can be defined the pulse functions as follows:

$$S_{abc} = \begin{bmatrix} S_a \\ S_b \\ S_c \end{bmatrix} = \sqrt{\frac{2}{3}} D \begin{bmatrix} \sin(\omega_e t) \\ \sin\left(\omega_e t - \frac{2\pi}{3}\right) \\ \sin\left(\omega_e t + \frac{2\pi}{3}\right) \end{bmatrix} \quad (\text{A. 6})$$

Where  $S_a, S_b, S_c$  are the equivalent switches respectively for phase ‘‘a’’:  $S_{a1}$  and  $S_{a2}$ , phase B:  $S_{b1}$  and  $S_{b2}$  and phase C:  $S_{c1}$  and  $S_{c2}$ .

The voltages supplied by the inverter, considering only the fundamental component of the voltage (i.e. in the absence of harmonics), are expressed in terms of the DC link voltage and the switching functions as:

$$v_{oabc} = \begin{bmatrix} v_{oa} \\ v_{ob} \\ v_{oc} \end{bmatrix} = \begin{bmatrix} S_a \\ S_b \\ S_c \end{bmatrix} v_{dc} \quad (\text{A. 7})$$

Since the system is balanced, the Park transformation of equation (A.7) is written as:

$$v_{oqd} = \begin{bmatrix} v_{oq} \\ v_{od} \end{bmatrix} = Dv_{dc} \begin{bmatrix} 0 \\ 1 \end{bmatrix} \quad (\text{A. 8})$$

Where  $D$  is the inverter conversion ratio between the fundamental of the output voltage and the DC voltage [37]:

$$D = \frac{\sqrt{v_{od}^2 + v_{oq}^2}}{v_{dc}} \quad (\text{A. 9})$$

The magnitude MI is given by:

$$MI = \frac{v_{o,\max}}{v_{dc}} = \sqrt{\frac{2}{3}} D \quad (\text{A. 10})$$

Substituting (A.3) and (A.8) into (A.5) gives:

$$\frac{d}{dt} \begin{bmatrix} i_q \\ i_d \end{bmatrix} = \begin{bmatrix} -\frac{R_f}{L_f} & -\omega_e \\ \omega_e & -\frac{R_f}{L_f} \end{bmatrix} \begin{bmatrix} i_q \\ i_d \end{bmatrix} + \frac{1}{L_f} \begin{bmatrix} -V_s \sin \delta \\ V_s \cos \delta + Dv_{dc} \end{bmatrix} \quad (\text{A. 11})$$

Based on the previous assumptions, the DC link current is:

$$i_{dc1} + i_{dc2} = 2i_{dc} = S^T i_{abc} \quad (\text{A. 12})$$

In the (d, q) axes:

$$2i_{dc} = S^T M_p i_{qdo} = D \begin{bmatrix} 0 & 1 & 0 \end{bmatrix} \begin{bmatrix} i_q \\ i_d \\ i_o \end{bmatrix} \quad (\text{A. 13})$$

Where  $M_p$  is the Park transformation matrix:

$$M_p = \sqrt{\frac{2}{3}} \begin{bmatrix} \cos(\omega_e t) & \cos\left(\omega_e t - \frac{2\pi}{3}\right) & \cos\left(\omega_e t + \frac{2\pi}{3}\right) \\ \sin(\omega_e t) & \sin\left(\omega_e t - \frac{2\pi}{3}\right) & \sin\left(\omega_e t + \frac{2\pi}{3}\right) \\ \frac{1}{\sqrt{2}} & \frac{1}{\sqrt{2}} & \frac{1}{\sqrt{2}} \end{bmatrix} \quad (\text{A. 14})$$

The voltage on the capacitor is given by:

$$\frac{dv_{dc}}{dt} = \frac{i_{dc}}{C_{dc}} \quad (\text{A. 15})$$

Combining equations (A.13) and (A.15) gives:

$$\frac{dv_{dc}}{dt} = \frac{D}{2C_{dc}} i_d \quad (\text{A. 16})$$

Finally, combining equation (A.16) with equations (A.11), yields the following nonlinear Park model of the source current and DC link voltage.

$$\frac{d}{dt} \begin{bmatrix} i_q \\ i_d \\ v_{dc} \end{bmatrix} = \begin{bmatrix} -\frac{R_f}{L_f} & -\omega_e & 0 \\ \omega_e & -\frac{R_f}{L_f} & -\frac{D}{L_f} \\ 0 & \frac{D}{2C_{dc}} & 0 \end{bmatrix} \begin{bmatrix} i_q \\ i_d \\ v_{dc} \end{bmatrix} + \frac{1}{L_f} \begin{bmatrix} -V_s \sin \delta \\ V_s \cos \delta \\ 0 \end{bmatrix} \quad (\text{A. 17})$$

## APPENDIX B: Linearised model of the grid-side.

From the state equation (A.15), it can be seen that the control parameter  $\delta$  takes the form of  $\sin \delta$  and  $\cos \delta$ . In addition, the state matrix depends on the inverter conversion ratio  $D$  which is not constant. Therefore, the system is non-linear. The reactive component of the current  $i_q$  of the source is zero (the system is operating at unity power

factor), in this case phase shift  $\delta$  between the fundamental voltages of the source and those of the inverter output voltage is almost zero ( $\delta \approx 0$ ). The model can therefore be linearized based on the following assumptions [38]:

- ✓ The second order terms of the perturbed variables are neglected.
- ✓ The value  $\delta_0$  operating point is zero.

The  $\Delta$ -notation is introduced to indicate perturbed values.

Applying a small perturbation to the system gives:

$$\left\{ \begin{array}{l} \dot{i}_{q0} + \dot{i}_{q\Delta} = -\frac{R_f}{L_f} [i_{q0} - i_{q\Delta}] - \omega_e [i_{d0} - i_{d\Delta}] + \frac{1}{L_f} [v_{q0} + v_{q\Delta}] \\ \dot{i}_{d0} + \dot{i}_{d\Delta} = \omega_e [i_{q0} - i_{q\Delta}] - \frac{R_f}{L_f} [i_{d0} - i_{d\Delta}] + \frac{1}{L_f} \{ [v_{d0} + v_{d\Delta}] - [v_{od0} + v_{od\Delta}] \} \\ \dot{v}_{dc0} + \dot{v}_{dc\Delta} = (D + D_\Delta) [v_{dc0} + v_{dc\Delta}] - D v_{dc0} \end{array} \right. \quad (\text{A.18})$$

Where the Park transformation of the source voltage and the inverter output voltages are given by [38]:

$$\left\{ \begin{array}{l} v_{q\Delta} + v_{q0} = -V_s \sin(\delta_0 + \delta_\Delta) + V_s \sin(\delta_0) \\ v_{d\Delta} + v_{d0} = V_s \cos(\delta_0 + \delta_\Delta) - V_s \cos(\delta_0) \\ v_{od\Delta} - v_{od0} = (D + D_\Delta) [v_{dc0} + v_{dc\Delta}] - D v_{dc0} \end{array} \right. \quad (\text{A.19})$$

Using the trigonometric development of  $\sin(\delta_0 + \delta_\Delta)$  and  $\cos(\delta_0 + \delta_\Delta)$ , equations (A.19) become:

$$\left\{ \begin{array}{l} v_{q\Delta} + v_{q0} = -V_s [\sin(\delta_0) \cos(\delta_\Delta) - \sin(\delta_\Delta) \cos(\delta_0)] + V_s \sin(\delta_0) \\ v_{d\Delta} + v_{d0} = V_s [\cos(\delta_0) \cos(\delta_\Delta) + \sin(\delta_0) \sin(\delta_\Delta)] - V_s \cos(\delta_0) \\ v_{od\Delta} - v_{od0} = (D + D_\Delta) [v_{dc0} + v_{dc\Delta}] - D v_{dc0} \end{array} \right. \quad (\text{A.20})$$

Quantities with subscript 0 are equal to those of the initial conditions ( $\delta_0 = 0$ ). Using the following approximations [39]:

$$\left\{ \begin{array}{l} \sin \delta_\Delta \approx \delta_\Delta \\ \cos \delta_\Delta \approx 1 \end{array} \right. \quad (\text{A.21})$$

The linearised model of the system (A.20) can be written as:

$$\left\{ \begin{array}{l} v_{q\Delta} + v_{q0} = -V_s \delta_\Delta \\ v_{d\Delta} + v_{d0} \approx 0 \\ v_{od\Delta} - v_{od0} \approx D v_{dc0} + D_\Delta v_{dc\Delta} \end{array} \right. \quad (\text{A.22})$$

Substituting equations (A.20) into (A.18), and assuming that the initial value of the current source is zero gives:

$$\left\{ \begin{array}{l} \frac{di_{q\Delta}}{dt} = -\frac{R_f}{L_f} i_{q\Delta} - \omega_e i_{d\Delta} - \frac{V_s}{L_f} \delta_\Delta \\ \frac{di_{d\Delta}}{dt} = \omega_e i_{q\Delta} - \frac{R_f}{L_f} i_{d\Delta} - \frac{1}{L_f} [-D v_{dc\Delta} + D_\Delta v_{dc0}] \\ \frac{dv_{dc\Delta}}{dt} = \frac{D}{2C_{dc}} i_{d\Delta} \end{array} \right. \quad (\text{A.23})$$

Finally, the linearised state-space model of the MIMO system can be written in matrix form as:

$$\frac{dx}{dt} = Ax + Bu \quad (\text{A.24})$$

Where:

$x$  is the state vector  $x = [i_{qd} \ i_{d\Delta} \ v_{dc\Delta}]^T$ , and  $u$  is the input vector  $u = [\delta_{\Delta} \ D_{\Delta}]^T$ .

$A$  and  $B$  are the state matrix and control or input matrix respectively and are given by

$$A = \begin{bmatrix} -\frac{R_f}{L_f} & -\omega_e & 0 \\ \omega_e & -\frac{R_f}{L_f} & -\frac{D}{L_f} \\ 0 & \frac{D}{2C_{dc}} & 0 \end{bmatrix}, \quad B = \frac{1}{L_f} \begin{bmatrix} -V_s & 0 \\ 0 & v_{dc0} \\ 0 & 0 \end{bmatrix} \quad (\text{A.25})$$

The system transfer matrix is calculated using :

$$G(s) = \frac{Y}{U} = C(sI - A)^{-1}B \quad (\text{A.26})$$

$$G(s) = \frac{\begin{bmatrix} -\frac{V_s}{L_f} \left( s^2 + \frac{R_f}{L_f} s + \frac{D^2}{2L_f C_{dc}} \right) & -\frac{\omega_e v_{dc0} s}{L_f} \\ -\frac{\omega_e V_s s}{L_f} & \left( s^2 + \frac{R_f}{L_f} s \right) \frac{v_{dc0}}{L_f} \\ -\frac{\omega_e V_s D}{2L_f C_{dc}} & \left( s + \frac{R_f}{L_f} \right) \frac{D v_{dc0}}{2L_f C_{dc}} \end{bmatrix}}{s^3 + 2 \left( \frac{R_f}{L_f} \right) s^2 + \left( \frac{D^2}{2L_f C_{dc}} + \left( \frac{R_f}{L_f} \right)^2 + \omega_e^2 \right) s + \frac{D^2 R_f}{2L_f^2 C_{dc}}} \quad (\text{A.27})$$

## APPENDIX C: Model parameters.

TABLE E. Models parameters values.

<b>Grid</b>	
RMS voltage, $V_s$ [V]	380
Frequency, $f_s$ [Hz]	50
<b>Transformer</b>	
Leakage resistance, $R_f$ [ $\Omega$ ]	3.4
Leakage inductance, $L_f$ [ $\Omega$ ]	3.3
<b>Turbine</b>	
Air density, $\rho$ [ $\text{Kg.m}^{-2}$ ]	1.225
Rated power, $P_{t,n}$ [kW]	2.68
Radius, $R$ [m]	1.4
Rated wind speed, $v_n$ [ $\text{m.s}^{-1}$ ]	12
Gain of Gearbox, $G$	2.445312
<b>SCIG</b>	
Rated power, $P_n$ [kW]	2
Rated frequency, $f_{g,n}$ [Hz]	50
Stator resistance, $R_s$ [ $\text{m}\Omega$ ]	4850
Stator leakage inductance, $L_{ls}$ [mH]	16
Rotor resistance, $R_r$ [ $\text{m}\Omega$ ]	3805
Rotor leakage inductance, $L_{lr}$ [mH]	16

Mutual inductance, $L_m$ [mH]	258	
Inertia, $J$ [kg.m <sup>2</sup> ]	0.031	
Friction factor, $f$ [N.m.sec.rad <sup>-1</sup> ]	0.00114	
Number of pole pairs, $p$	2	
<b>DTC-SVM</b>		
SVM switching frequency [Hz]	2000	
<b>PI controllers</b>		
	$K_p$	$K_i$
<b>Generator</b>		
Speed controller	1	15.872
Torque controller	2	150
Flux controller	200	1200
<b>DC side</b>		
DC voltage controller	2	25
<b>Source side</b>		
Current controller	6	4500
<b>Pitch control</b>		
Pitch controller	5000	2
Maximum pitch angle [deg]		45
Maximum rate of change of pitch angle [deg/sec]		10

## References

- [1] Half-year Report, WWEA, The World Wind Energy Association, pp. 1-7, 2013.
- [2] S. K.Hyong, L. Dylan Dah-Chuan, "Wind Energy Conversion System from Electrical Perspective - A Survey," *Smart Grid and Renewable Energy*, Vol.1, No.3, November, pp. 119-131. 2010.
- [3] R. Rechsteiner, "Wind power in context - A clean revolution in the energy sector", Energy Watch Group / Ludwig – Boelkow - Foundation, Decembre 2008. ([www.energywatchgroup.org](http://www.energywatchgroup.org)).
- [4] A. Haejoon, K. Heesang, K. Hongwoo, K. Hyungoo, K. Seokwoo and all. "Modelling and voltage-control of variable-speed SCIG-based wind farm," *Renewable Energy* 42, June 2012: pp28-35.
- [5] J.L. Domínguez García, O. Gomis Bellmunt, L. Trilla-Romero, A. Junyent-Ferré, "Vector control of squirrel cage induction generator for wind power," *IEEE XIX International Conference on Electrical Machines ICEM'10*, 6-8 Sept. 2010, Rome. pp 1 – 6.
- [6] A. Haejoon, K. Heesang, K. Hongwoo, K. Seokwoo, J. Gilsoo, L. Byongjun, "Modeling and voltage-control of variable-speed SCAG-based wind farm," *International Symposium on Low Carbon and Renewable Energy Technology ISLCT'10*, *Renewable Energy*, Vol.42, June 2012: pp 28-35.
- [7] H. S. Kim and D. D.-C. Lu, "Wind energy conversion system from electrical perspective - A survey," *Smart Grid and Renewable Energy*, Vol. 1 Issue 3, pp 119-131, 2010.
- [8] C. N. Bhende, S. Mishra, and S. G. M. Tanaka, "Permanent magnet synchronous generator-based standalone wind energy supply system," *IEEE Trans. Sustainable Energy* 2(4), pp 361-373 2011,.
- [9] M. E. Haque, M. Negnevitsky, and K. M. Muttaqi, "A novel control strategy for a variable-speed wind turbine with a permanent-magnet synchronous generator," *IEEE Trans. Ind. Appl.* 46(1), pp 331-339, 2010.

- [10] E.B. Muhando, T. Senjyu, A. Uehara, T. Funabashi "Gain-Scheduled  $H_\infty$  Control for WECS via LMI Techniques and Parametrically Dependent Feedback Part II: Controller Design and Implementation,". IEEE Transactions on Industrial Electronics, Vol. 58 Issue 1, pp 57-65, 2011.
- [11] A. Mesemanolis, C. Mademlis, I. Kioskeridis, "Maximum electrical energy production of a variable speed Wind Energy Conversion System," IEEE 21st International Symposium on Industrial Electronics ISIE'12, Hangzhou china, 28- 31 May 2012, pp 1029-1034.
- [12] Y. Xing-Jia, G. Chang-Chun, L. Yan, "LPV H-infinity Controller Design for Variable-Pitch Variable-speed Wind Turbine," IEEE 6th International Conference on Power Electronics and Motion Control, IPEMC '09, 17-20 May 2009, Wuhan, China, pp 2222 – 2227.
- [13] V. J. Ginter, J. K. Pieper, "Robust Gain Scheduled Control of a Hydrokinetic Turbine Part1: Design," IEEE Energy Conference on Electrical Power EPEC'09, 22-23 Oct. Montreal, Canada, 2009, pp: 1-6.
- [14] Z. Dengying, "LVP H-infinity Controller Design for a Wind Power Generator," 2008 IEEE Conference on Robotics, Automation and Mechatronics, 21-24 September, Chengdu, China, 2008, pp 873 – 878.
- [15] K. Lahmadi, S. Aboulem, and I. Boumhidi, "LMI Conditions to Design a Robust Fuzzy Controller for a Wind Generator", 5th IEEE International Conference on Systems and Control, ICSC'16, Marrakesh, Morocco, 25-27 May, 2016. pp: 312-318, 2016.
- [16] K. Prakash Ray, P. Singh Vijay, R. Mohanty Soumya and all; "Frequency Control Based on  $H_\infty$  Controller for Small Hybrid Power System," IEEE 5th International Conference on Power Engineering and Optimization PEOCO'11,-Selangor, Malaysia: 6-7 June 2011, pp: 227–232.
- [17] G.D. Moor; H.J. Beukes, "Maximum power point trackers for wind turbines," IEEE 35th Annual Conference on Power Electronics Specialists, PESC'04, vol.3, 20-25 June 2004, Aachen, Germany, pp. 2044- 2049.
- [18] H. Merabet Boulouiha, A. Allali, A. Tahri, A. Draou, and M. Denai, "A simple maximum power point tracking based control strategy applied to a variable speed squirrel cage induction generator," J. Renewable Sustainable Energy Vol. 4, Issue 5, 053124 (2012), doi:10.1063/1.4763562.
- [19] M. Pardalos Panos, R. Steffen, V. F. Pereira Mario, A. Iliadis Niko, P. Vijay, "Handbook of Wind Power Systems" Book Series Energy Systems, Springer-Verlag, 2013.
- [20] H. Merabet Boulouiha, A. Allali, M. Laouer, A. Tahri, M. Denai, and A. Draou, "Direct torque control of multilevel SVPWM inverter in variable speed SCIG-based wind energy conversion system," Renewable Energy, Vol. 80, August 2015, pp: 140–152.
- [21] D.W. Gu, I. Postlethwaite, M.C. Tsai "H $\infty$  Super Optimal Solutions. Advances in Control and Dynamic Systems," Vol 51, Academic Press, San Diego, pp. 183-246, 1992.
- [22] J.C Doyle., K. Glover, P.K. Khargnekar, B.A. Francis "State-Space Solution to standard  $H_2$  and  $H_\infty$  control problem," IEEE Transactions on Automatic Control, Vol. 34, pp 831-846, 1989.
- [23] P. Apkarian, J.M. Biannic, P. Gahinet "Self-scheduled  $H_\infty$  Control of Missile via Linear Matrix Inequalities," Journal of Guidance, Control and Dynamics, vol. 18, N° 3, pp. 532-538, 1995.
- [24] P. Gahinet, P. Apkarian "A Linear Matrix Inequality Approach to  $H_\infty$  Control", International Journal of Robust and Nonlinear Control, Vol. 4, Issue 4, pp 421–448, 1994
- [25] C. Scherer, "The Riccati Inequality and State-Space  $H_\infty$  Optimal Control", Ph.D Thesis, University of Wurzburg, Germany, 1990.
- [26] C. Scherer, P. Gahinet, and M. Chilali, "Multi-objective output-feedback control via LMI optimization," IEEE Trans. Autom. Control, vol. 42, N° 7, pp. 896-911, 1997.

- [27] J. Sabatier, P. Lanusse, P. Melchior, A. Oustaloup, 'Fractional Order, Differentiation and Robust Control Design CRONE, H-infinity and Motion Control' Book Series in Intelligent Systems, Control and Automation: Science and Engineering, Springer, 2015.
- [28] H. Jahangir, P. Hemanshu Roy, "Robust Control for Grid Voltage Stability: High Penetration of Renewable Energy", Power System, Springer, pp 1-17, 2014.
- [29] Y. Sun, Su Mei, W. H. Gui, "One novel Variable-speed wind energy system based on PMSG and super sparse matrix converter," IEEE International Conference on Electrical Machines and Systems, ICEMS'08, 17-20 october 2008, Wuhan, China, pp.2384–2389.
- [30] T. Nakamura, S. Morimoto, M. Sanada, Y. Takeda, "Optimum control of IPMSG for wind generation system" Conference on Power Conversion, PCC'02, Vol. 3, 2-5 April 2002, Osaka, pp.1435 -1440.
- [31] G. Abad, J. Lopez, M. A. Rodriguez, L. Marroyo, and G. Iwanski, "Doubly Fed Induction Machine: Modeling and Control for Wind Energy Generation" Wiley-IEEE Press, 2011.
- [32] S. Heier, "Grid Integration of Wind Energy: Onshore and Offshore Conversion Systems, 3rd Edition, Wiley, 2014.
- [33] P. Van Dooren, E. Fridman, U. Shaked "H<sub>∞</sub> control of linear state-delay descriptor systems: an LMI approach' Linear Algebra and its Applications," Vol. 351–352, 15 August 2002, Fourth Special Issue on Linear Systems and Control, pp 271–302, 2002
- [34] G.C. Cho, N. S. Choi, C.T. Rim, and G. H. Cho, "Modeling, Analysis and Control of Static Var Compensator Using Three-Level Inverter," IEEE Conference on Industry Applications Society Annual Meeting, Vol.1, pp. 837-943, 1992.
- [35] H. Fujita, S. Tominaga, and H. Akagi, "Analysis and Design of a DC Voltage-Source Inverters," IEEE Transactions on Industry Applications, Vol.32, N°4, pp. 970-978, 1996.
- [36] M.T. Bina and M.D. Eskandari, "Consequence of Unbalance Supplying Condition on a Distribution StaticCompensator," IEEE 35th Annual Conference on Power Electronics Specialists, PESC'04. Vol.5, 20-25 June 2004, Aachen, Germany, pp 3900–3904.
- [37] A. J. Calvaer, "Voltage Stability and Collapses: a Simple Theory Based on Real and Reactive Currents," RGE: Revue Generale D'Electricite-N°8, 1986, pp: .1-17
- [38] C. Cho Guk, H. Jung Gu, S. Choi Nam and H. Cho Gyu, "Control of VAR Compensator (SVC) With DC Voltage Regulation and Fast Dynamics By Feedforward and Feedback loop," IEEE\_26th Conference on Power Electronics, PESC'95, Vol.1, 18-22 June 1995, pp. 367 – 374.
- [39] S Frank, S Rebennack, "An Introduction to Optimal Power Flow: Theory, Formulation, and Examples", IIE Transactions, Vol. 0, Issue 0, May 2016 - Taylor & Francis.